4

Shrinkage induced flow during directional solidification of pure substance in a bottom cooled cavity: A study on flow reversal phenomena

4.1 INTRODUCTION

Phase change processes associated with solidification and melting is an intrinsic component of manufacturing processes like casting and welding, and thermal management applications involving latent heat thermal energy storage, cyclic cooling of electronic equipment. The physics associated with solidification process is multi-scale in nature, spanning from nano to macro scale. State of the art manufacturing technologies like additive manufacturing processes involving laser sintering, laser surface alloying essentially deal with melting and re-solidification mechanisms. Numerous complex flow physics involving marangoni convection due to surface tension [Dutta et al., 1995; Sarkar et al., 2002; Raj et al., 2002; Kashchiev, 2003], natural convection, shrinkage convection [Zhang and Faghri, 1999; Chen and Zhang, 2006; Xiao and Zhang, 2006] play key role in defining the desirable mechanical properties of the products manufactured through such advanced processes. Thus, understanding of such flow physics is of utmost importance to obtain improved product yield from these processes. The broad area of primitive, contemporary and advanced manufacturing applications pertinent to melting and solidification process instigated commendable research outcomes by several research groups over the past few decades.

Regardless of clarity in definition, the issues associated with the solidification are complex to perceive. The foremost concern related to solidification phenomenon is to track the evolving solid-liquid interface. There exists three classes of solidification process, namely, (a) distinct, (b) alloy and (c) continuous. Distinct solidification process involves existence of a sharp interface between solid and liquid phases, typically featuring solidification of pure metals. Alloy solidification process involves regions of columnar and equi-axed crystalline structures with complex shapes of solid-liquid interface, and typically encountered during the solidification of metal alloys. For the continuous solidification process, the individual phases are dispersed in every part of the phase change region and no distinct interface exists. Typical examples of continuous solidification process are freezing of oil, wax and polymers. Distinct interface tracking can be achieved by well established front tracking method [Unverdi and Tryggvason, 1992; Tryggvason et al., 2001; De Sousa et al., 2004], level set method [Sussman et al., 1998], and marker and cell method [Harlow and Welch, 1965]. However, for alloy and continuous solidification processes interface is hardly distinct,and the tracking methods are computationally expensive and difficult to implement [Voller et al., 1990]. One of the reliable schemes to address all three types of solidification processes is fixed grid based enthalpy or volume fraction updating method. The major advantage of fixed grid enthalpy updating method [Voller et al., 1990] is the redundancy of explicit coupling requirements for energy and mass balance at the interface location. Considerable number of numerical models involving well-established enthalpy updating scheme to solve pure metal or binary alloy solidification have been reported by several researchers [Voller et al., 1987; Voller and Prakash, 1987; Brent et al., 1988; Swaminathan and Voller, 1992, 1993; Chakraborty, 2017].

The enthalpy updating formulation for capturing solid-liquid interface during

solidification of pure metals and binary alloys was originally proposed by Voller et al. [1987]; Voller and Prakash [1987]. The key feature of the formulation proposed by Voller et al. [1987]; Voller and Prakash [1987] are the inclusion of local variation of latent heat of fusion as a source term in the energy conservation equation, and the iterative evolution of the same. Brent et al. [1988] proposed a farther modification of the model originally proposed by Voller et al. [1987]; Voller and Prakash [1987], and reported that a faster convergence is possibly obtained for the solidification under the effect of natural convection by using enthalpy porosity approach. Recently, Chakraborty [2017] proposed a modified enthalpy updating method which evaluates solid or liquid volume fraction and simulates phase change process of materials with substantial variation between phase specific heats.

All the enthalpy updating based solidification models proposed till date has the limitation of considering same density of liquid and solid phases. Shrinkage or volumetric expansion effects due to the difference of liquid and solid phases is an important aspect of solidification process for most of the pure substances and alloys. The incorporation of the effects of different phase densities within the present framework of the enthalpy updating scheme will lead to a more reliable numerical scheme to predict evolution of all three types of solidification processes. Existing solidification models involving shrinkage effect are rarely found [Xu and Li, 1991; Chiang and Tsai, 1992b,a; Krane and Incropera, 1995]. Among the few existing models involving shrinkage effect, the pioneering model was proposed by Chiang and Tsai [1992b,a]. The analysis reported by Chiang and Tsai [1992b,a] involves directional solidification from bottom side of 1 % Cr-Steel in a rectangular cavity with a riser at the center. This particular configuration was chosen to suppress all other possibilities of natural convection due to side [Kefayati, 2019] and top cooling [Satbhai et al., 2019], while shrinkage induced flow takes the lead role in shaping the solid front growth. However, the absence of source term associated with natural convection in the analysis reported by Chiang and Tsai [1992b], nullified any possibility of interaction between the buoyancy and shrinkage induced source terms from the modeling point of view. The possibility of such interaction needs to be explored further. The study of shrinkage induced convection is particularly crucial, since convection in the liquid and mushy regions plays a key role in enhancing or suppressing casting defects like macro-segregation, porosity and hot tears [Flemings, 1974]. Experiments involving directional solidification with bottom cooling configuration are performed to study macro-segregation [Kato and Cahoon, 1985; Rerko et al., 2003; Ferreira et al., 2004, 2009], grain growth of metals and their alloys [Ziv and Weinberg, 1989; Alkemper et al., 1998; Gandin, 2000a], and convection owing to density anomaly of fluid [Kumar et al., 2017, 2018c, 2019]. To the best knowledge of the present authors, no experimental study addressed shrinkage induced flow and its effect on solid front growth till date.

Based on the existing literature survey, following objectives are postulated and studied: (a) Improvement of existing enthalpy updating scheme by incorporating shrinkage effect; (b) investigation of shrinkage induced flow and its effect on solid front growth during continuous and distinct solidification process; (c) investigation on interaction between the shrinkage induced source term and buoyancy source term; (d) exploring the possibility of implementing pressure boundary condition within the Semi-Implicit Method for Pressure-Linked Equations Revised (SIMPLER) algorithm frame work [Versteeg and Malalasekera, 2007]; (e) quantitative and qualitative validation of the proposed model with experimental findings. The numerical model presented in the chapter is limited to predict the effect of shrinkage induced flow on solid front growth during distinct and continuous directional solidification processes associated with pure metals, oils, wax, and other polymeric substances, and not alloys. However, evolution of mushy zone is accounted for, since oils, wax, and other polymeric substances freezes over a fixed temperature range. Hence, up-gradation of the proposed model for predicting alloy solidification is expected to be attainable and is discussed in succeeding chapter. For two dimensional (2-D) numerical analysis, solidification of pure aluminium (Al) and copper (Cu) is studied whereas; for

3-D numerical and experimental investigations, solidification of coconut oil is studied.

4.2 MATHEMATICAL MODELING

The physical domain for which the numerical and experimental investigations are performed, is shown in figure 4.1. The physical domain is set in a similar fashion as reported by Chiang and Tsai [1992b] to address the effect of shrinkage induced flow during directional solidification from bottom surface. The domain consists of a rectangular cavity with a riser at the center (figure 4.1). The cavity is initially filled with liquid material above freezing temperature range ($T_i > T_L$). Solidification ensues as the temperature of the bottom wall is set below the solidus temperature (T_S). All other sides of the cavity are insulated. It is assumed that the riser is continuously fed with liquid melt from a source tank located above the riser. The volume averaged continuum formulation of mass, momentum balance originally proposed by Bennon and Incropera [1987a], and later modified by Chiang and Tsai [1992b] to incorporate shrinkage effect have been used for the present numerical model. The volume fractions of liquid and solid phases are defined as g_l, g_s respectively, while the liquid and solid mass fractions are estimated to be: $f_l = g_l\rho_l/\rho$ and $f_s = g_s\rho_s/\rho$ respectively. For both volume and mass fractions $g_l + g_s = 1$, and $f_l + f_s = 1$. It is assumed that thermo-physical properties are different for liquid and solid phases. However, for individual phases, these properties do not vary with temperature. As shrinkage effect is considered, liquid and solid phases have different densities ($\rho_s \neq \rho_l$). Defining volume averaged density: $\rho = g_l\rho_l + g_s\rho_s$, and mass averaged velocity as: $\vec{V} = f_l\vec{V}_l + f_s\vec{V}_s = (g_l\rho_l/\rho)\vec{V}_l + (g_s\rho_s/\rho)\vec{V}_s$, the conservation equations for mass and momentum are given as follows [Bennon and Incropera, 1987b; Chiang and Tsai, 1992b]:

Continuity

$$\frac{\partial}{\partial t}(\rho) + \nabla.\left(\rho\vec{\mathbf{V}}\right) = 0 \tag{4.1}$$

Momentum

$$\frac{\partial}{\partial t}(\rho u) + \nabla.\left(\rho\vec{\mathbf{V}}u\right) = \nabla.\left(\mu_l\frac{\rho}{\rho_l}\nabla u\right) - \frac{\partial p}{\partial x} - \frac{\mu_l}{K}\frac{\rho}{\rho_l}u - \nabla.\left(\rho\frac{g_s\rho_s}{g_l\rho_l}\vec{\mathbf{V}}u\right) + \nabla.\left(\mu_l u\nabla\left(\frac{\rho}{\rho_l}\right)\right) \tag{4.2}$$

$$\frac{\partial}{\partial t}(\rho v) + \nabla.\left(\rho\vec{\mathbf{V}}v\right) = \nabla.\left(\mu_l\frac{\rho}{\rho_l}\nabla v\right) - \frac{\partial p}{\partial y} - \frac{\mu_l}{K}\frac{\rho}{\rho_l}v - \nabla.\left(\rho\frac{g_s\rho_s}{g_l\rho_l}\vec{\mathbf{V}}v\right) + \nabla.\left(\mu_l v\nabla\left(\frac{\rho}{\rho_l}\right)\right) + \rho^l_{ref}g_a\beta_T\left(T - T_{ref}\right) \tag{4.3}$$

The fifth term appearing on the right hand side of u and v momentum conservation Eqns. 4.2 and 4.3 represent the source term associated with shrinkage effect. This particular source term solely accounts for the shrinkage induced fluid flow during the solidification process. The fourth term appearing on the right hand sides of Eqns. 4.2 and 4.3 represent inertial forces within the mushy region where liquid volume fraction varies within the range of $0 < g_l < 1$. The third term on the right side of Eqns. 4.2 and 4.3 represent the Darcian damping force term for porous medium; once again of relevance only within the mushy region. The effect of the inertia terms are typically found out to be negligible as compared to the Darcian damping term [Bennon and Incropera, 1987a; Chiang and Tsai, 1992b]. However, for the sake of generality the inertia term has been retained for the present model. K appearing in the Darcian damping force source terms is defined as follows [Bennon and Incropera, 1987b]:

$$K = K_0\left(\frac{g_l^3 + \varepsilon}{(1 - g_l)^2}\right) \tag{4.4}$$

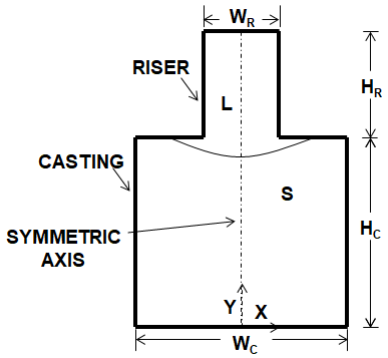

Figure 4.1 : Schematic of the physical domain of interest.

where, ε is a very small number ($\sim 10^{-8}$) to restrain Darcian term from blowing off numerically as $g_l \to 0$, and K_0 is the permeability constant. The last term appearing on the right hand side of v-momentum Eq. 4.3 represents the natural convection or buoyancy term in the liquid melt. Where, ρ^l_{ref}, g_a, β_T are the reference melt density, gravitation alacclereation and thermal expansion coefficient of the melt respectively. It is important to mention here, that Chiang and Tsai [1992b] excluded the buoyancy source term from their analysis during bottom cooling configuration; and thereby nullifying any chance of interaction between the shrinkage induced source term and buoyancy source term. They [Chiang and Tsai, 1992a] however, included the buoyancy source term for the side cooling case study. The conservation equations are formulated on the assumption that the phase velocity within solid remains immobile, i.e. $\vec{V}_s = 0$.

The energy conservation equation is again derived on the basis of volume averaged continuum formulation originally proposed by Bennon and Incropera [1987a]. Mass averaged enthalpy is defined as $h = f_l h_l + f_s h_s$, where h_s and h_l are respective phase enthalpies in solid and liquid defined as: $h_s = c_{ps}T$ and $h_l = (c_{ps} - c_{pl})T_S + h_{sl} + c_{pl}T$. c_{ps} and c_{pl} are specific heat capacities for solid and liquid phases respectively. T_S is the solidus temperature of the amorphous substance. The energy equation is expressed in terms of temperature as the scalar variable, rather than volume averaged enthalpy [Chakraborty, 2017]. The latent heat appears in conjunction with liquid volume fraction in one out of three source terms of the energy conservation Eq. 4.5. The fourth term appearing on the right hand side of energy conservation Eq. 4.5 also contains liquid volume fraction. It is to be noted that two out of three source terms (second and fourth term) in energy conservation Eq. 4.5 appears if there exists a difference between liquid and solid specific heats, and both of these source terms vanish when liquid and solid phases have same specific heat capacity, i.e. $c_{ps} = c_{pl}$. A volume fraction updating method is employed to estimate the solid/liquid volume fraction over the entire domain to capture solid, mushy (containing dispersed solid and liquid phases) and liquid regions. The mushy region is defined by a temperature range within liquidus (T_L) and solidus (T_S) (upper and lower limits of freezing temperature range) temperatures respectively. The conservation of energy is given as follows [Chakraborty, 2017]:

Energy

$$\frac{\partial}{\partial t}(\rho T) + \nabla.\left(\rho \vec{\mathbf{V}} T\right) = \nabla.\left(\frac{k}{c_{ps}}\nabla T\right) - \nabla.\left[\left(\frac{c_{pl}}{c_{ps}} - 1\right)\rho \vec{\mathbf{V}} T\right] - \frac{\partial}{\partial t}\left(\frac{\rho_s g_l h_{sl}}{c_{ps}}\right) - \frac{\partial}{\partial t}\left[g_l\left(\frac{c_{pl}}{c_{ps}} - 1\right)(\rho_l T - \rho_s T_S)\right] \quad (4.5)$$

Since the solidification configuration depicted in figure 4.1 contains lateral symmetry with respect to the central line, computations were performed for one of the symmetric halves in order to reduce the overall computational time. The boundary conditions for solving momentum and energy conservation Eqns. 4.2, 4.3 and 4.5 are given as: (1) at top face:- $\partial u/\partial y = 0$, gauge pressure $p = 0$,

$\partial T/\partial y = 0$; (2) at left face (symmetric axis):- $u = 0$, $\partial v/\partial x = 0$, $\partial T/\partial x = 0$; (3) at bottom wall:- $u = 0$, $v = 0$, $T = T_c$; and (4) at all the remaining walls:- $u = 0$, $v = 0$, thermally insulated.

4.3 NUMERICAL APPROACH AND VOLUME FRACTION UPDATING METHODOLOGY

The governing equations (Eq. 4.1, 4.2, 4.3 and 4.5) associated with fluid flow and heat transfer during directional solidification, are in conservative form [Patankar, 2018]. They contain a transient term, a diffusive term, a convective term, and source terms pertinent to the physics of macro-scale solidification process. The finite volume approach of discretization converts this system of parabolic partial differential equations (Eq. 4.1, 4.2, 4.3 and 4.5) into a system of linear algebraic equations [Patankar, 2018]. The systems of these linear algebraic equations are then solved iteratively over the entire domain for each time step. Semi-implicit iterative method is used for solving coupled velocity and temperature fields. Coefficients associated with combined convection and diffusion terms are formulated using power law scheme [Patankar, 2018; Versteeg and Malalasekera, 2007]. Although power law scheme is more complicated as compared to hybrid scheme in implementation, it is computationally less expensive, and provides a better representation of exponential behaviour observed for combined convection diffusion problems. For 2-D analysis, the fourth and fifth source terms appearing on the right hand side of Eq. 4.2 and Eq. 4.3, as well as the second source term appearing on the right hand side of Eq. 4.5 are discretized by using implicit first order upwind scheme. In order to check the accuracy of the first order upwind scheme, few of the initial simulations are also performed considering second order upwind scheme (Linear upwind difference scheme or LUDS [Stansby, 2003]), and results obtained with these two schemes are compared. However, difference between the simulated results using first order and second order upwind schemes are found to be insignificant. Since, implementation of second order upwind scheme is computationally more expensive as compared to first order upwind scheme, first order upwind scheme is chosen to handle convective source terms for all subsequent numerical simulations. Line-by-line tridiagonal matrix algorithm (TDMA) solver is used to solve the system of linearly discretized algebraic equations for each of field variables, namely u, v and T. 'Semi-Implicit Method for Pressure Linked Equations Revised' (SIMPLER) algorithm is chosen to solve momentum and continuity equations simultaneously for obtaining the velocity field. The choice of SIMPLER algorithm over more frequently used SIMPLE algorithm is made to obtain improved convergence rate of the solver.

For SIMPLER [Patankar, 2018] algorithm, the pressure boundary condition at the top face is applied by setting pressure equal to zero at inner grid points adjacent to the physical boundary. During the evaluation of pressure correction at these inner grid points adjacent to the physical boundary with constant pressure boundary condition, source terms S_C and S_P in the discretized linear algebraic pressure correction equation are set to be zero, and coefficient a_p is set to have a very large value ($\sim 10^{30}$)[Patankar, 2018; Versteeg and Malalasekera, 2007]. As a result, the combined effect of other coefficients (a_E, a_W, a_N and a_S) is suppressed in the discretized linear algebraic pressure correction equation, and numerically attained pressure correction values are ~ 0. Vertical velocity component v at the location of zero gauge pressure boundary condition is computed by using mass conservation at the grid points ($v_N + u_E - v_S - u_W = 0$) [Versteeg and Malalasekera, 2007].

For 3-D analysis, user defined function for the source terms corresponding to momentum equations were incorporated in ANSYS 18.1. The default energy equation of ANSYS was turned off, and instead Eq. 4.5 is implemented by declaring T as user defined scalar. The gradients present in source terms were evaluated using Green-Gauss cell based method [Fluent, 2017]. For each time-step the velocity field is predicted first from the guessed pressure, density, and volume fractions, followed by the prediction of temperature field. Finally, phase volume fractions and

densities are re-evaluated using newly updated temperature field. For each time step, iterations are continued until velocity and temperature satisfies the absolute convergence criteria [ANSYS, 2017] of 10^{-5} and 10^{-6} respectively.

The volume fraction updating is somewhat trivial for continuous solidification process of amorphous material defined by fixed values of liquidus (T_L) and solidus (T_S) temperatures. However, for solidification of pure substance with distinct solid-liquid interface, updating of g_l is not trivial and calls for a novel numerical scheme. For the present work, g_l updating methods are derived for both continuous and distinct interface type solidification processes.

For continuous solidification process g_l is defined in the following manner.

$$g_l = \begin{cases} 1 & \text{for } T \geq T_L \\ 0 < g_l < 1 & \text{for } T_S < T < T_L \\ 0 & \text{for } T \leq T_S \end{cases} \tag{4.6}$$

Liquid volume fraction (g_l) at a node point is simply calculated as:

$$g_{l_P}^{n+1} = \frac{T_P^n - T_S}{T_L - T_S} \tag{4.7}$$

However, to ensure numerical convergence, the following iterative formulation is considered.

$$g_{l_P}^{n+1} = g_{l_P}^n + \lambda \left[\frac{T_P^n - T_S}{T_L - T_S} - g_{l_P}^n \right] \tag{4.8}$$

Where, subscript P represents the node point, superscripts n and $n+1$ denote subsequent iteration steps and λ is a under-relaxation factor.

Updating of g_l is however more demanding when solidification of pure substance with distinct solid-liquid interface and constant freezing point needs to be addressed. For solidification of pure substance the liquid phase enthalpy is defined as $h_l = (c_{ps} - c_{pl})T_m + h_{sl} + c_{pl}T$, with T_m being the distinct freezing temperature. Thus, T_S appearing in the last source term on the right hand side of energy equation (Eq. 4.5) has to be replaced with T_m. For solidification with distinct interface the volume fraction at the liquid, solid and interface region is defined in the following manner.

$$g_l = \begin{cases} 1 & \text{for } T > T_m + \varepsilon \\ 0 \leq g_l \leq 1 & \text{for } T = T_m \pm \varepsilon \\ 0 & \text{for } T < T_m - \varepsilon \end{cases} \tag{4.9}$$

Where, ε is a small number ($O \sim 10^{-6}$), and a physical representation of permissible overheating or under-cooling at the interface location [Chakraborty, 2017]. The volume fraction updating is derived on the basis of similar approach proposed by Voller and Prakash [1987]. To obtain an exclusive relation to update g_l, Eq. 4.5 is discretized into a linear algebraic equation using finite volume method, and is given as follows:

$$\left(a_P + a_P^{'}\right) T_P = \sum \left(a_{nb} + a_{nb}^{'}\right) T_{nb} + A_P^0 g_{l_P}^0 - A_P g_{l_P} + B_P^0 g_{l_P}^0 (\rho_l T_P^0 - \rho_s T_m) - B_P g_{l_P} (\rho_l T_P - \rho_s T_m) + a_P^0 T_P^0 \tag{4.10}$$

$a_P^{'}$ and $a_{nb}^{'}$ appearing in Eq. 4.10 are the coefficients obtained by discretizing the second term on the right hand side of Eq. 4.5 using first order upwind scheme. Whereas, a_P and a_{nb} are evaluated using power law scheme defined by Patankar [2018] and superscript 0 denotes previous time-step values. Noting $a_P = a_E + a_W + a_N + a_S + a_P^0$, Eq. 4.10 can be rearranged and expressed for n^{th} iteration step as follows,

$$a_P^0 T_P^n = (A)^n + (B)^n + (C)^n + (D)^n \tag{4.11}$$

where,

$$(A)^n = \sum \left(a_{nb} + a'_{nb}\right)^n (T_{nb})^n - \left(a_E + a_W + a_N + a_S + a'_P\right)^n T_P^n \tag{4.12}$$

$$(B)^n = A_P^0 g_{l_P}^0 + B_P^0 g_{l_P}^0 \left(\rho_l T_P^0 - \rho_s T_m\right) + a_P^0 T_P^0 \tag{4.13}$$

$$(C)^n = -(A_P)^n g_{l_P}^n \tag{4.14}$$

$$(D)^n = -(B_P)^n g_{l_P}^n (\rho_l T_P - \rho_s T_m)^n \tag{4.15}$$

Similarly, for $n+1^{th}$ iteration step Eq. 4.10 is reordered as,

$$a_P^0 T_P^{n+1} = (A)^{n+1} + (B)^{n+1} + (C)^{n+1} + (D)^{n+1} \tag{4.16}$$

$(A)^{n+1}$, $(B)^{n+1}$, $(C)^{n+1}$ and $(D)^{n+1}$ is evaluated by replacing n with $n+1$ in Eqns. 4.12-4.15. By subtracting Eq. 4.16 from Eq. 4.11, and noting $(B)^{n+1} = (B)^n$, it is obtained,

$$a_P^0 T_P^n - T_P^{n+1} = \left[(A)^n - (A)^{n+1}\right] + \left[(C)^n - (C)^{n+1}\right] + \left[(D)^n - (D)^{n+1}\right] \tag{4.17}$$

At this point, a drastic measure of dropping the first term on the right hand side of Eq. 4.17 involving convection-diffusion terms is taken. At first glance, dropping of the convection-diffusion term looks severe, however, in an iterative framework this decision leads to a permissible and convenient updating method for g_l. Dropping the combined convection-diffusion flux effects renders Eq. 4.17 to retain only the transient terms.

$$a_P^0 \left(T_P^n - T_P^{n+1}\right) = \left[(C)^n - (C)^{n+1}\right] + \left[(D)^n - (D)^{n+1}\right] \tag{4.18}$$

A_P, B_P and a_P^0 appearing in Eqns. 4.10-4.18 are given as follows [Patankar, 2018].

$$A_P = \frac{\rho_s h_{sl}}{c_{ps}} \frac{\Delta x \Delta y}{\Delta t} \; ; B_P = \left(\frac{c_{pl}}{c_{ps}} - 1\right) \frac{\Delta x \Delta y}{\Delta t} \text{ and } a_P^0 = \frac{\rho_P^0 \Delta x \Delta y}{\Delta t} \tag{4.19}$$

Noting (from Eq. 4.19) that, $(A_P). = (A_P)^{n+1}$ and $(B_P)^n = (B_P)^{n+1}$, and substituting expressions of C and D from Eqns. 4.14 and 4.15 in Eq. 4.18 following expression appears for updating g_l.

$$g_{l_P}^{n+1} = g_{l_P}^n + \frac{\left[B_P \rho_l g_{l_P}^n + a_P^0\right]\left(T_P^n - T_P^{n+1}\right)}{A_P + B_P \left(\rho_l T_P^{n+1} - \rho_s T_m\right)} \tag{4.20}$$

An elementary control volume undergoing solidification process needs to satisfy the condition of attaining freezing temperature T_m. Thus, T_P^{n+1} is chosen to be T_m in Eq. 4.20. Additionally, an under-relaxation factor λ is multiplied with the second term appearing on the right hand side of Eq. 4.20. As a result, $g_{l_P}^{n+1}$ is evaluated by adding a correction factor with the previous iteration value $g_{l_P}^n$.

$$g_{l_P}^{n+1} = g_{l_P}^n + \lambda \frac{\left[B_P \rho_l g_{l_P}^n + a_P^0\right]\left(T_P^n - T_m\right)}{A_P + B_P T_m \left(\rho_l - \rho_s\right)} \tag{4.21}$$

Eqns. 4.8 and 4.21 provides the required volume fraction updating formulations for solidification processes associated with continuous and distinct interface solid front growth. Finally, considering the fact that physical value of volume fraction remains within the range $0 \leq g_l \leq 1$, values of g_l obtained from the proposed formulation (Eqns. 4.8 and 4.21) are restricted to exist within this permissible range by assigning following conditions:

$$g_{l_P}^{n+1} = \begin{cases} 1 & \text{if } g_{l_P}^{n+1} > 1 \quad \text{from Eq. 4.8 or 4.21} \\ 0 & \text{if } g_{l_P}^{n+1} < 0 \quad \text{from Eq. 4.8 or 4.21} \end{cases} \tag{4.22}$$

Thus, a very comprehensible volume fraction updating scheme (Eqns. 4.8, 4.21 and 4.22) is developed which allows us to estimate volume fraction ahead of calculating the velocity and temperature fields.

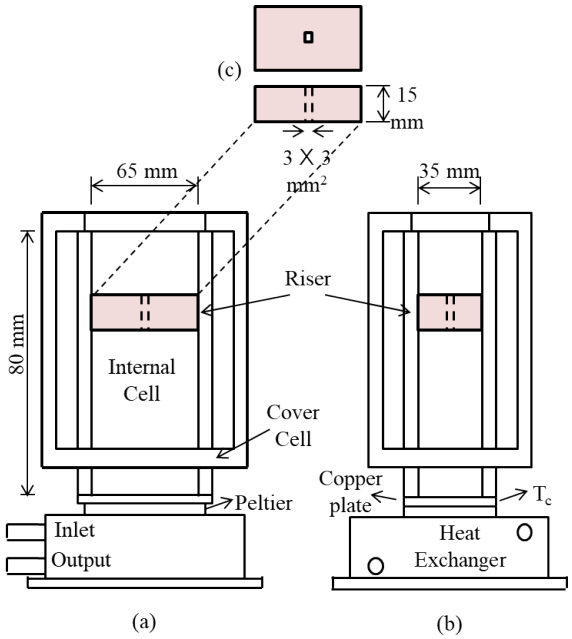

Figure 4.2 : Schematic of experimental setup (a) Front view, (b) Side view and (c) Riser.

4.4 EXPERIMENTAL SETUP

To validate the numerical results associated with the proposed shrinkage induced flow model, an experimental setup is designed and fabricated to study the solidification of coconut oil in a bottom cooled configuration. The experiments are performed to obtain both qualitative and quantitative validation. One of the major limitations of the present numerical model is its incapability of capturing the evolution of free surface (the interface between liquid and air at the top of the riser). Thus, the riser needs to have a steady supply of melt from a larger reservoir during the solidification process. Suitable arrangements are incorporated in the experimental setup to meet this particular feature.

The schematic of experimental setup is shown in figure 4.2. The experimental set up consists of a rectangular cavity divided into an upper and a lower cell by a thick acrylic glass. The acrylic glass separating the two cavities contains a through and through square hole at the center, which acts as a connecting riser between the upper and lower cavities. The upper cavity serves as the melt reservoir, while the lower one represents the solidification cell. The bottom most surface of the lower cavity is cooled below the solidus temperature (T_S) of coconut oil, and solidification ensues from this surface. All the side walls of the cavity are adequately insulated by maintaining an air gap between the inner wall and outer wall of the central cavity [Kumar et al., 2018c].

The flow physics associated with shrinkage induced convection is similar for all three types of solidification processes (distinct interface type, continuous and alloy solidification). However, coconut oil is chosen on basis that (a) it is transparent in liquid phase, (b) the range of freezing temperature is close to room temperature ($T_L = 300\ K$ and $T_S = 294\ K$ for coconut oil), and (c) the density difference between solid and liquid phases is fairly large ($\rho_s - \rho_l = 60\ kg/m^3$) to induce shrinkage driven flow during solidification process. Since the velocity field in the melt is captured by using Particle Image Velocimetry (PIV), transparency of the liquid phase is an absolute necessity for experimental visualization of the velocity field.

The inner and outer walls of the cavity are built using acrylic glass of 8 *mm* thickness. The dimension of the rectangular inner cavity is $65 \times 35 \times 80$ *mm* (length×thickness×height), and the overall dimension of the rectangular exterior of the setup is $101 \times 71 \times 70$ *mm*. Provision is made to separate the inner cavity into upper and lower chambers by means of placing a solid block acrylic glass of dimension $65 \times 35 \times 15$ *mm* inside the cavity. The solid block connecting

Table 4.1 : Material properties for Al [Gandin, 2000b; Dinsdale and Quested, 2004], casting conditions and geometrical data for numerical analysis (refer figure 4.1)

$k_l = 90.7\ W/mK$	$k_s = 211\ W/mK$
$c_{pl} = 1087\ J/kgK$	$c_{ps} = 1203\ J/kgK$
$\rho_l = 2370\ kg/m^3$	$\rho_s = 2535\ kg/m^3$
$h_{sl} = 398000\ J/kg$ (*)	$\beta_T = 2.1 \times 10^{-5}\ K^{-1}$ (*)
$\mu = 1.38 \times 10^{-3}\ kg/m\ s$	$T_m = 933.2\ K$
$T_i = 1073\ K$	$T_c = 800\ K$
$W_c = 200\ mm$	$H_c = 100\ mm$
$W_R = 20\ mm$	$H_R = 50\ mm$

* Assumed.

the upper and lower cavities contains a square hole of 3×3 *mm* through the block at the center and is merely the minimum geometrical constraint achievable by laser cutter. The square hole connecting the upper and lower cavities functions as a riser, and allows fluid to flow from upper to lower cavity to compensate for the shrinkage of the melt encountered in the lower cavity due to ongoing solidification process in it. The vertical positioning of the separating solid block with riser hole is made adjustable, so that the volume of the reservoir and solidification chamber can be altered as per the experimental requirements. Solidification is obtained by maintaining cooling temperature ($T_c < T_S$) of a 2 *mm* thick Cu plate located at the bottom of the lower cavity. In order to maintain a fixed cooling temperature T_c at the bottom surface of the lower cavity, Peltier modules (Thermo-electric cooler modules) integrated with Cu chill heat exchanger [Kumar et al., 2017, 2018b] is used. Thermal conductivity of acrylic glass is very low ($< 0.2\ W/mK$). The air gap maintained between the inner and outer walls all around the cavity enhances the insulation farther, causing negligible heat transfer from the surrounding. For flow visualization in the melt, the liquid coconut oil initially occupying the lower solidification chamber and upper reservoir cavity is seeded with neutrally buoyant hollow glass spheres of 10 μm average diameter. Once solidification ensues from the bottom most surface of the lower cavity, PIV (MicroVec PIV ®) technique is used to capture velocity field in the melt[Kumar et al., 2017, 2018b].

4.4.1 Experimental procedure

Coconut oil is heated to a temperature of 308 *K* to make sure that at the initial state it is in pure liquid phase. The ambient temperature in the room is controlled and maintained at 308 *K* using number of heaters and thermostats. Seed particles are added into the liquid coconut oil at 308 *K* and stirred till uniform distribution of seed particles in the melt is obtained. The seeded liquid coconut oil is then poured into the rectangular cavity and stirred thoroughly, ensuring no air pocket is trapped in the liquid at any part of the cavity. The separating block containing the connecting through and through hole is then placed. Position of the separating block is adjusted to obtain desired volume of solidification chamber. As solidification process ensues and continues, images of the 2-D field obtained from the Laser-Mirror arrangement [Kumar et al., 2017, 2018c] are captured continuously using charged coupled device (CCD) camera ((Imperx CLB-B2520M, resolution 2456×2048). PIV images are captured using the magnification of $8\times$ and a pulse width of 125 *ms*. While evaluating the velocity field from the images by MicroVec PIV software, an interrogation window of 64×32 pixel was chosen [Kumar et al., 2017, 2018b,a]. The sequential image data are stored in a memory drive and TECPLOT software is used for data processing and velocity field image recreation. During the experiments, the bottom surface temperature of solidification cell is maintained at 258 *K*.

4.5 RESULTS AND DISCUSSION

This section is divided into three subsections. First subsection involves comparison of 2-D shrinkage induced flow with and without considering buoyancy effect. The shrinkage induced flow analysis reported by Chiang and Tsai [1992b] involving directional solidification from bottom was devoid of buoyancy effect consideration. Our first objective is to check the merit of this particular assumption in predicting the shrinkage induced flow field. The analysis involves obtaining shrinkage induced flow field and solid front growth during directional solidification of pure Al with bottom cooled configuration. The results obtained in this subsection shows that inclusion of buoyancy source term alters the flow field significantly as opposed to that obtained without including the buoyancy effect. Second subsection is attributed to experimental validation of the flow phenomena obtained from the numerical results in the first subsection. The experimental validation involves directional solidification of coconut oil in bottom cooled configuration. Qualitative and quantitative validation of the proposed model is discussed in this subsection. The third subsection is attributed to the 2D case studies involving solidification of pure Cu and Al to verify the generality of this newly found orientation. The study involving directional solidification of Al is revisited with varying parameters such as cold boundary temperature, initial temperature, and cavity aspect ratio.

4.5.1 Comparison 2-D shrinkage models with and without considering buoyancy effect

Numerical analysis is carried out for directional solidification of pure Al in a bottom cooled configuration considering (a) exclusion of buoyancy effect on flow field [Chiang and Tsai, 1992b], and (b) inclusion of buoyancy effect on flow field. Properties of pure Al are shown in table 4.1 along with casting conditions and cavity geometry details. In order to study grid independence, analysis is carried out for three different grid sizes namely; 60×90, 80×120, and 100×150 for the symmetry half. Similarly, the time step independence is checked by considering three different time steps namely $\Delta t = 0.25$, 0.5, and 1.0 s. Maximum velocity (v_{max}) within the fluid domain and the interface position (y_{int}) from the bottom surface of the cavity along the symmetry-axis obtained at the time instant 10 s are compared and tabulated in table 4.2 for different grid sizes, and time steps. No significant difference in results is found above grid size 80×120 and time step below Δt=0.5 s (the results differ within 1% error limit). Hence, a grid size of 80×120 grids and time step Δt=0.5 s are used for most of the 2-D case studies. For the case studies involving varying aspect ratio of the cavity, the grid size is modified in a proportionate manner. Figure 4.3 shows velocity fields and solid fronts at different stages of solidification when buoyancy effect is not considered. For this case study, similar flow fields to that described by Chiang and Tsai [1992b] are obtained (figure 4.3). The flow fields shown in figure 4.3 is characterized by a single descending fluid column coming straight down from the riser, which eventually collides head on with the growing solid front before getting bifurcated into two counter rotating convection cells. The maximum velocity within the flow field is mentioned at the top of the each figure.

On the other hand, when the buoyancy effect is taken into account, the evolution of flow

Table 4.2 : Grid independence study for 2-D numerical analysis at time 10 s; comparison of maximum flow velocity v_{max} and solid-liquid interface location y_{int}

Grid size \ time step		0.25 s	0.5 s	1 s
60×90	$v_{max}(mm/s)$	–	1.114	–
	$y_{int}(mm)$		17.32	
80×120	$v_{max}(mm/s)$	1.101	1.080	0.912
	$y_{int}(mm)$	17.511	17.557	17.797
100×150	$v_{max}(mm/s)$	–	1.091	–
	$y_{int}(mm)$		17.472	

field shown in figure 4.4 indicates a distinctively different flow pattern. As is evident from the flow fields shown in figure 4.4, the fluid column entering the cavity from the riser cannot penetrate deeper into the melt region of the cavity. Instead, the incoming fluid column gets bifurcated in the lateral direction just after entering the cavity to once again produce a pair of counter rotating convection cells. However, the counter rotating convection cells obtained from this analysis have exactly opposite directionality as compared to those obtained from the no buoyancy effect consideration. Figure 4.5 provides a schematic representation of the two different flow fields obtained from these two analysis. For bottom cooling configuration the density field is stably stratified. As a result, cold and heavier fluid layers adjacent to the growing solid front resists downward movement of the hot and lighter incoming fluid from the riser. In essence, the stably stratified buoyancy field opposes the shrinkage induce flow to penetrate deeper into the melt region. Consequently, the incoming fluid from the riser is forced to take a least resistant lateral path at an early stage of its descent from the riser. As a result, the incoming flow from the riser is bifurcated at a region adjacent to the riser opening, forming pair of counter rotating convection cells in 2-D plane. The very nature of the flow causes the heavier cold fluid close to the solid front to rise along the central column and collide head on with the down-coming flow from the riser opening leading to the sustenance of this typical flow field. From comparison of flow fields obtained after 10 s without and with buoyancy effect (figure 4.3(a) and 4.4(a)), both the flow fields look identical with partial penetration of the descending fluid column from the riser opening into the cavity. However, at later stages of solidification (figure 4.3(b), (c) and 4.4(b), (c)) the flow fields obtained from these two case studies exhibit highly contrasting flow reversal pattern.

Since the bottom cooled orientation typically provides a stably stratified density field in the vertical direction, effect of buoyancy can only be evident if there exists non horizontal isotherms along x direction. Figure 4.4(d) and (e) show the vertical and horizontal non-dimensional temperature profiles at chosen values of x and y coordinate locations respectively at time instant 100 s. As is evident, the vertical temperature profiles represented by figure 4.4(d) indicate stably stratified density field along the vertical direction (low temperature corresponding to higher density and high temperature corresponding to lower density). However, temperature profile in horizontal direction is found to be undulated justifying the significance of buoyancy effect. We should note here that the non-dimensioning of temperature (in figure 4.4(d) and (e)) is executed by considering maximum and minimum temperatures along the chosen vertical and horizontal lines only and not through global maximum or minimum temperatures. A close view of figure 4.4(e) indicates that the differences between these maximum and minimum temperatures are found to be quite small (typically of the order of 0.1 to 1 K). Evidently, the buoyancy force variation along the horizontal direction although small is nevertheless existing (figure 4.4(f)). At first glance, the buoyancy force profile along the horizontal direction (figure 4.4 (f)) gives an impression that the coupling torque should give rise to a pair of vortices with fluid coming down along the center line and rising along the side walls, which contradicts our present observation. However, we must remember, it is the combined effect of shrinkage and buoyancy that defines the flow field. As we have mentioned earlier, the incoming flow from the riser containing hot lighter fluid being

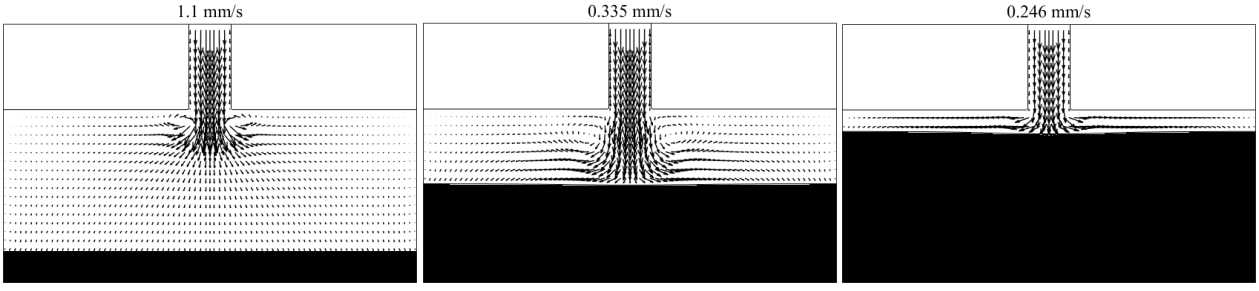

Figure 4.3 : Shrinkage induced flow field during solidification of pure Al in bottom cooled configuration without considering buoyancy effect; at times (a) 10 s, (b) 100 s, and (c) 200 s

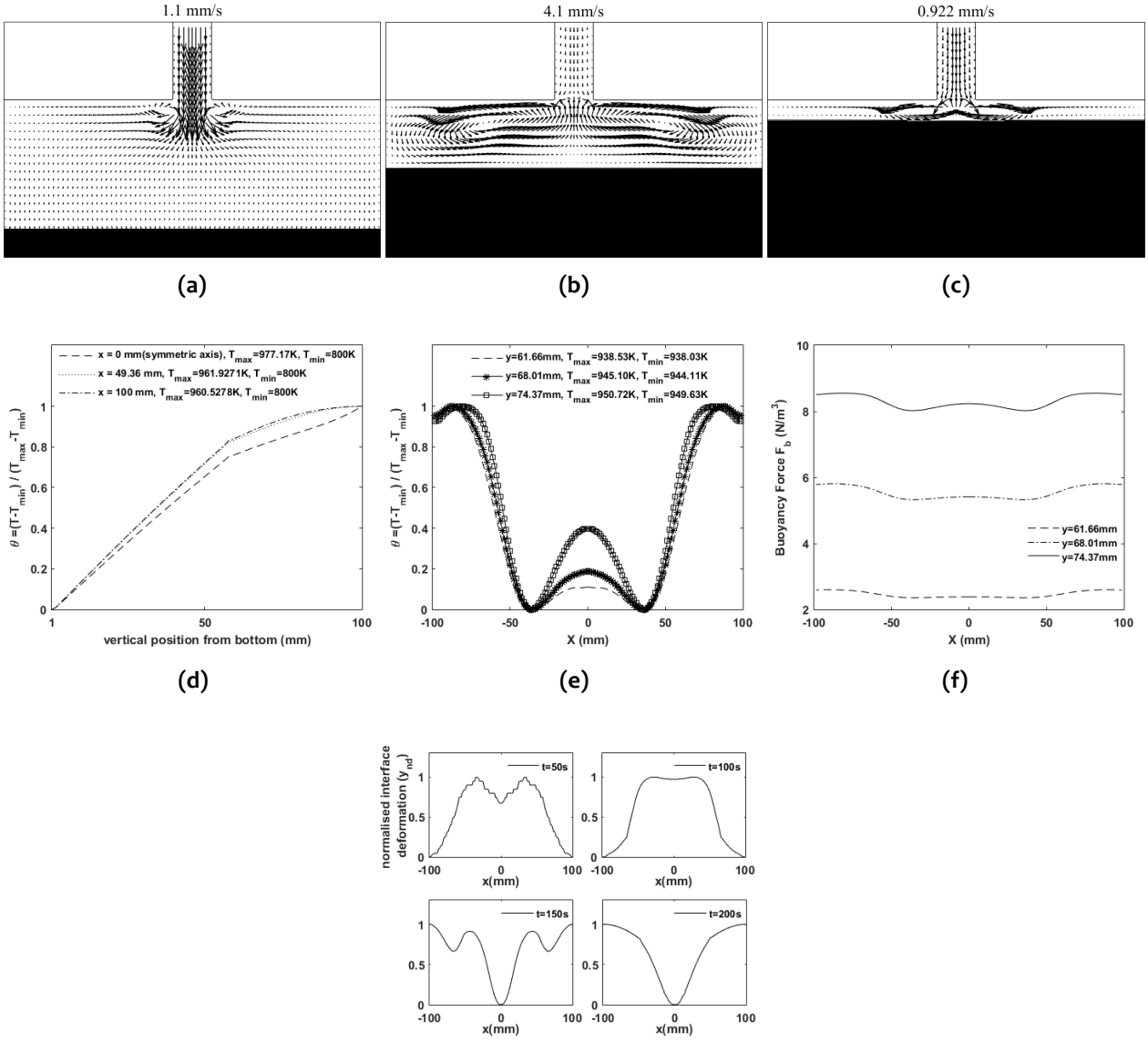

Figure 4.4 : Shrinkage induced flow field during solidification of pure Al in bottom cooled configuration considering buoyancy effect; at times (a) 10 s, (b) 100 s, and (c) 200 s; and the (d) temperature profile in y-direction at constant x-locations and time 100 s, (e) near interface temperature deformation in x-direction at constant y-locations and time 100 s, (f) buoyancy force (per unit volume: $\rho^{l}_{ref} g_a \beta_T (T - T_{ref})$ variation in x-direction at constant y-locations and time 100 s and (g) normalised interface deformation $(y_{nd} = (y_{int} - y_{int_{min}})/(y_{int_{max}} - y_{int_{min}}))$ at different times, where y_{int} represents the height of the interface from the bottom surface of the cavity; (t(s),$y_{int_{min}}$(mm),$y_{int_{max}}$(mm)):→(50, 38.8681, 38.8749)/ (100, 56.7189, 56.8621)/ (150, 73.0414, 73.1903)/ (200, 87.085, 87.8438).

unable to penetrate the colder heavy liquid layers lying immediately underneath chooses lateral paths with less flow resistance, and is driven towards the side walls. Adjacent to the side walls the shrinkage induced flow has no other option but to flow in the downward direction along the wall. The inertia of this shrinkage induced downward flow counteracts fluid region having higher buoyancy nullifying the buoyancy effect in that region. On the other hand, the buoyancy force in the vicinity of the cavity central line does not get counteracted by any such means. The inertia of the rerouted shrinkage induced flow following the cavity profile along the walls and interface towards the central line of the cavity ends up assisting the buoyancy force adjacent to the cavity center to lift the fluid from the interface along the center line. Figure4.4(g) provides close up view of the interface profile along horizontal direction at different time intervals. All these interface shapes are

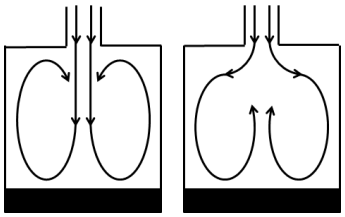

Figure 4.5 : Schematic of flow physics obtained (a) without accounting for buoyancy effect, and, (b) considering buoyancy effect

characterized by the presence of a central depression. This central depression becomes more and more prominent as the solid front grows with the passage of time. The minuscule deformation of isotherms adjacent to the central depression of the interface aided by the inertial effect of rerouted shrinkage induced flow causes the sustenance of reversed flow phenomena. A similar phenomena was observed during vertical Bridgman growth with bottom cooled configuration by Motakef [1990], although shrinkage induced flow was not as prominent as the present study.

4.5.2 Experimental validation

To comprehend the newly found flow physics, 3-D numerical and experimental studies were performed considering coconut oil as the phase change material (PCM). Thermo-physical properties of coconut oil reported by Timms [1985] are considered and tabulated in table 4.3 along with casting conditions. However, experimentally measured values of thermal conductivity of solid and liquid phases of coconut oil (k_l and k_s) are considered for the better accuracy of numerical prediction. Also, the data regarding the thermal expansion coefficient of coconut oil (β_T) being unavailable in existing literature, we assumed the numerical value of this parameter for our numerical prediction. For the experimental analysis, the solid block separating the upper and lower chambers is positioned to maintain the height of solidification cavity (lower chamber) at 40 mm. The numerical analysis is carried out for the one fourth symmetric portion, cut along the symmetry planes passing through the length and width of the solidification cavity and riser. For 3-D analysis, along with the Eq. 4.1, 4.2, 4.3 and 4.5, the momentum equation along z-axis (representing width of the cavity) is also solved. The z-momentum equation is given as follows.

$$\frac{\partial}{\partial t}(\rho w) + \nabla.\left(\rho \vec{\mathbf{V}} w\right) = \nabla.\left(\mu_l \frac{\rho}{\rho_l} \nabla w\right) - \frac{\partial p}{\partial z} - \frac{\mu_l}{K}\frac{\rho}{\rho_l} w - \nabla.\left(\rho \frac{g_s \rho_s}{g_l \rho_l} \vec{\mathbf{V}} w\right) + \nabla.\left(\mu_l w \nabla\left(\frac{\rho}{\rho_l}\right)\right) \quad (4.23)$$

The riser cross section is chosen to ascertain the magnitude of fluid velocity within the perceivable range of PIV measurement. For the numerical analysis, grid independence and time-step independence study is carried out. Three different grid resolutions are considered. After attaining satisfactory grid independence, three different time-steps are considered to investigate time-step independence for the chosen grid resolution. Mass flow rate at the riser inlet at the time instant 180 s during the solidification is compared for different grid resolutions and time-steps, tabulated in table 4.4. On the basis of this comparison, the second grid resolution depicted in table 4.4 with

Table 4.3 : Material properties for coconut oil and casting conditions for numerical analysis

$k_l = 0.2004\ W/mK$ (**)	$k_s = 0.3\ W/mK$ (**)
$c_{pl} = 2088\ J/kgK$	$c_{ps} = 2088\ J/kgK$
$\rho_l = 900\ kg/m^3$	$\rho_s = 960\ kg/m^3$
$h_{sl} = 108784\ J/kg$	$\beta_T = 8.9 \times 10^{-4}\ K^{-1}$ (*)
$\mu = 3.29 \times 10^{-2}\ kg/m\ s$	$T_S = 294\ K$
$T_L = 300\ K$	$T_i = 308\ K$
$T_c = 258\ K$	

* Assumed ** Measured

Table 4.4 : Grid independence study for 3-D numerical analysis at time 180 s

time step / Grid size		0.1 s	0.5 s	1 s
	$(36 \times 20 \times 40)^a$ $+(4 \times 4 \times 16)^b$	4.4504×10^{-7} kg/s	-	-
	$(54 \times 30 \times 60)^a$ $+(6 \times 6 \times 24)^b$	4.4532×10^{-7} kg/s	4.4508×10^{-7} kg/s	4.4323×10^{-7} kg/s
	$(63 \times 35 \times 70)^a$ $+(7 \times 7 \times 28)^b$	4.5397×10^{-7} kg/s	-	-

^{a} grid resolution for cavity ^{b} grid resolution for riser

time-step 0.5 s is selected for the numerical analysis.

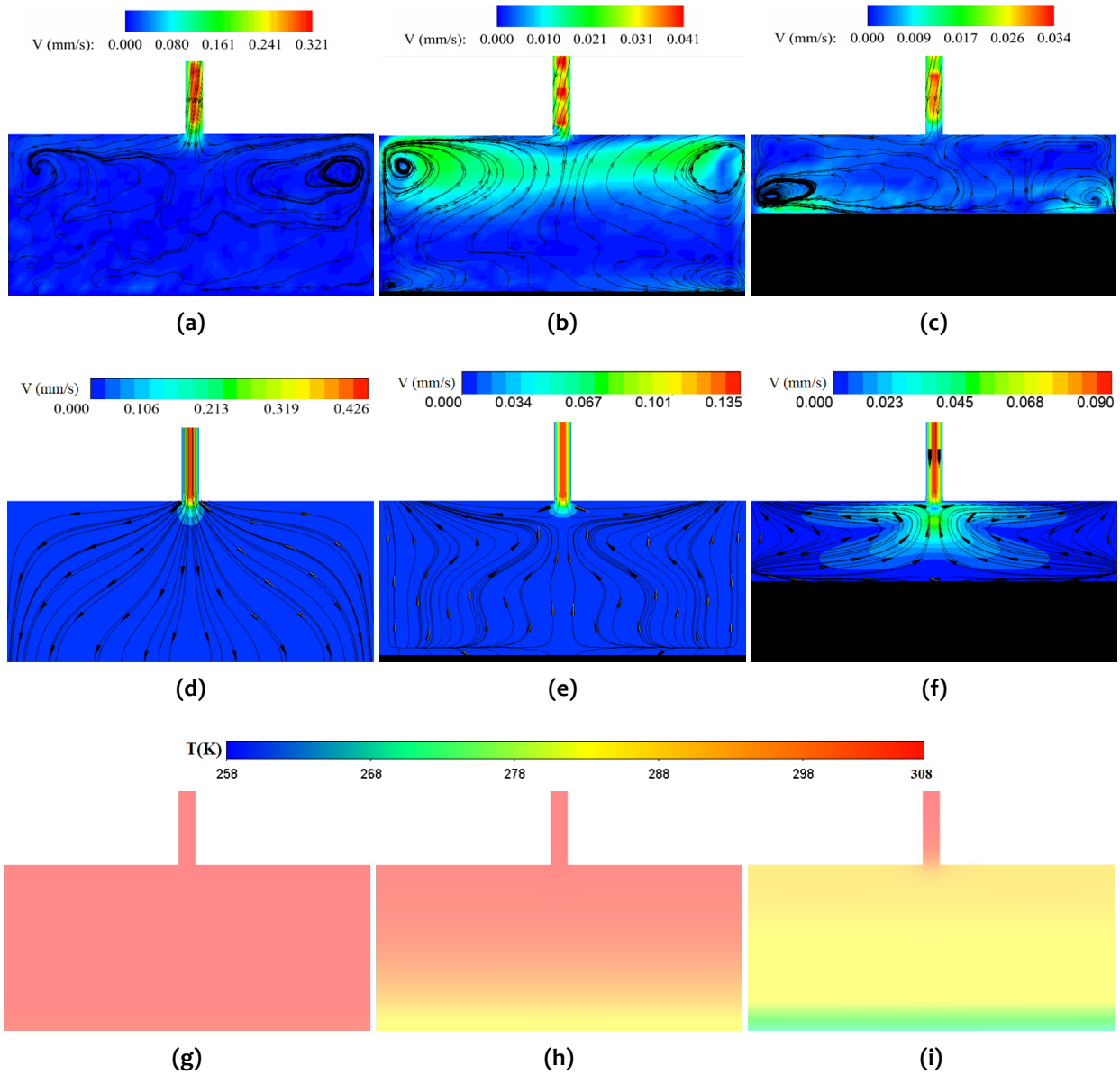

Figure 4.6 : Experimentally measured velocity field and mushy-liquid interface location at times: (a) 180 s, (b) 1200 s, and (c) 4500 s; Numerically obtained velocity field and mushy-liquid interface location at times: (d) 180 s, (e) 1200 s, and (f) 4500 s; and, Temperature field at times: (g) 180 s, (h) 1200 s, and (i) 4500 s respectively.

The velocity field and liquid-mushy zone interface locations obtained from experiments

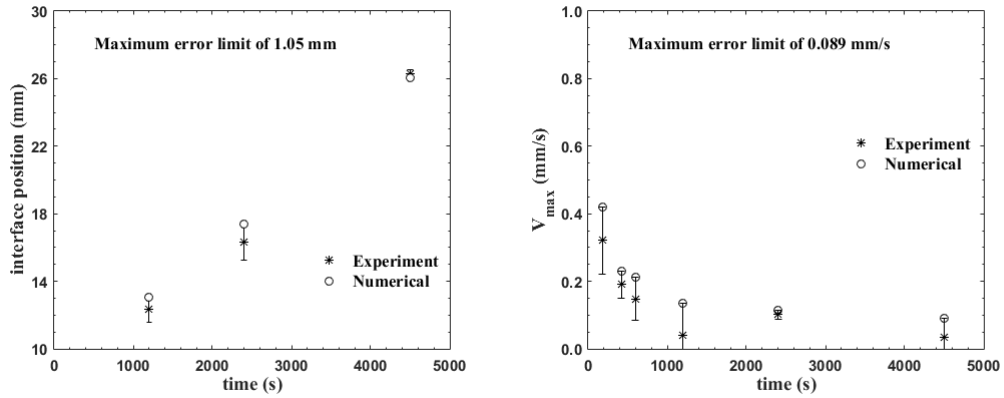

(a) (b)

Figure 4.7 : Comparison between experimentally and numerically obtained temporal variation of: (a) interface position, and (b) maximum velocity within the melt domain.

and numerical analysis are compared and shown in figure 4.6 during different stages of solidification of coconut oil. It is pertinent to mention here that the camera resolution of the PIV system restricted us to capture the entire cavity-riser arrangement. Hence, we chose only the upper portion of the solidification cavity along with the riser as our field of view (L = 65 mm × H = 30.7 mm). The experimental results shown in figure 4.6(a), (b) and (c) indeed confirm the reverse flow phenomena described by the simplified diagram presented in figure 4.5(b). The qualitative comparisons between experimentally and numerically attained flow patterns within the melt domain shown in figure 4.6 are found to agree reasonably. A quantitative validation between experimentally and numerically obtained temporal evolution of interface positions and magnitude of maximum velocities within the fluid domain is also carried out and shown in figure 4.7. Although we obtained a very good match between the experimentally measured and numerically determined interface location, the comparison of maximum absolute velocity is found out to be reasonable in terms of order of magnitude. The mismatches between experimental and numerical results can be attributed to the probable differences between the real and assumed values of thermo-physical properties, uncertainties associated with experiments, marginal errors in geometric considerations, and, minor heat losses through the side walls.

Unlike the 2-D case study involving bottom cooled directional solidification of pure aluminium, the flow reversal phenomena is found to be dominant from the very inception of the solid front growth during directional solidification of coconut oil with bottom cooled orientation. Liquid aluminium being a metal with significantly high thermal conductivity has a very low Prandtl number ($Pr = 0.0165$). Strength of Pr signifies the ability of flow field to perturb the thermal field. Prandtl number of liquid aluminium being very small, perturbation of thermal field due to shrinkage induced flow during directional solidification of aluminium is expected to be minuscule. However, minute deformation of isotherms due to the emergence of central depression of the solid-liquid interface (figure 4.4(g)) causes the unbalanced buoyancy force adjacent to the cavity central region to initiate the flow reversal phenomena. The flow reversal phenomenon for bottom cooled directional solidification of aluminium does not occur till the emergence of the central depression on solid-liquid interface. On the other hand, Prandtl number for coconut oil is found out to be quite large ($Pr = 342.8$), suggesting the possibility of significant deformation of thermal field due to the existing flow field. As a result, an undulated buoyancy field along the horizontal direction can be achieved even before the emergence of the non-planer of solid front, and flow reversal is prominent from the very instance of the solid front growth.

The interaction between convection field and liquid-mushy interface causes the interface to deviate from planer growth. Deformation of planer interface in the form of a plunge pool with length and width wise orientation is observed during the experiments. Figure 4.8 (a) and (b) show the orientation of these plunge pools during two different sets of experiments. The numerical

Table 4.5 : Material properties for Cu along with casting conditions for numerical analysis (refer figure 4.1)

$k_l = 180\ W/mK$	$k_s = 390\ W/mK$
$c_{pl} = 490\ J/kgK$	$c_{ps} = 390\ J/kgK$
$\rho_l = 7881\ kg/m^3$	$\rho_s = 8790\ kg/m^3$
$h_{sl} = 206000\ J/kg$	$\beta_T = 0.000016\ K^{-1}$
$\mu = 0.00321\ kg/m\ s$	$T_m = 1356\ K$
$T_i = 1496\ K$	$T_c = 1223\ K$
$W_c = 200\ mm$	$H_c = 100\ mm$
$W_R = 20\ mm$	$H_R = 50\ mm$

simulations could capture these experimentally manifested plunge pools with limited accuracy (figure 4.8(c)). However, the numerical prediction of the plunge pool is obtained after a time lag of approximately 120 s as compared to the experimental observations. The orientation of the plunge pools shown in figure 4.8(b) and (c) is found to be similar in nature. And the particular orientation of the plunge pool can be attributed to the square cross section of the riser, which allowed the shrinkage induced flow to align along the length and width of the cavity. The shrinkage induced deformity of planer mushy front in the form of distinctively oriented plunge pool might lead to interesting compositional heterogeneity during the solidification of alloy systems. However, directional alloy solidification is beyond the scope of this work.

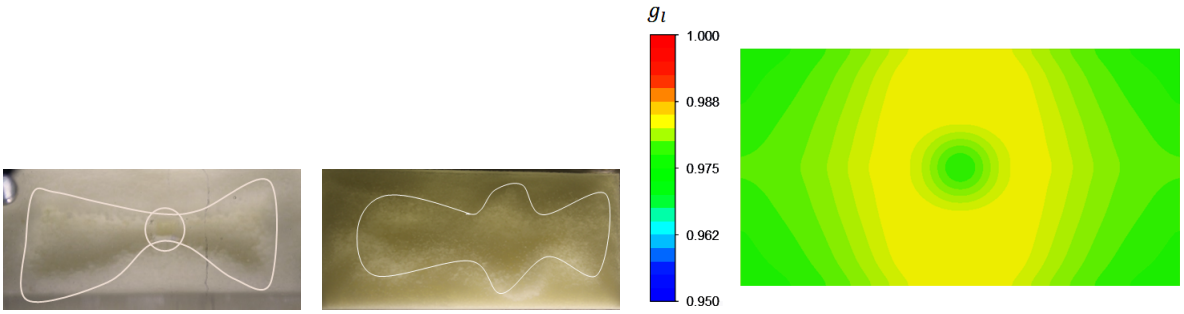

Figure 4.8 : Plunge pool orientation obtained from top view at the mushy-liquid interface caused by convection penetration for: (a) Experiment 1 at 5400 s, (b) Experiment 2 at 5400 s (c) Numerically predicted liquid volume fraction on the interface plane at 5520 s

4.5.3 Case studies

Once confidence on the proposed model is established through the experimental validation, analysis is performed considering directional solidification in bottom cooled orientation for one more pure metal namely Cu to check the generality of the proposed model. Finally, solidification of Al for various cold boundary temperatures, initial conditions and cavity heights are analysed.

Directional solidification of pure Cu

Associated thermo-physical properties and geometric data for Cu are provided in table 4.5 [Assael et al., 2010; Cahill and Kirshenbaum, 1962]. Same mesh size and time-step used for the 2-D analysis concerning solidification of pure Al in subsection 4.5.1 is used for this analysis. Initial temperature T_i and cold boundary temperature T_c for the analysis are selected in such a way that $T_i - T_m \approx 140\ K$ and $T_m - T_c \approx 133\ K$. Figure 4.9 shows the evolution of velocity field and interface growth at time instants 10 s, 24 s and 100 s. Temporal evolution of velocity field is found to be quite similar to that obtained for pure Al presented by figure 4.9. The flow field at an early stage is characterised by a pair of counter rotating convection cells adjacent to the riser opening with central plane flow directed in the downward direction (figure 4.9 (a), (b)). At later stages of solidification

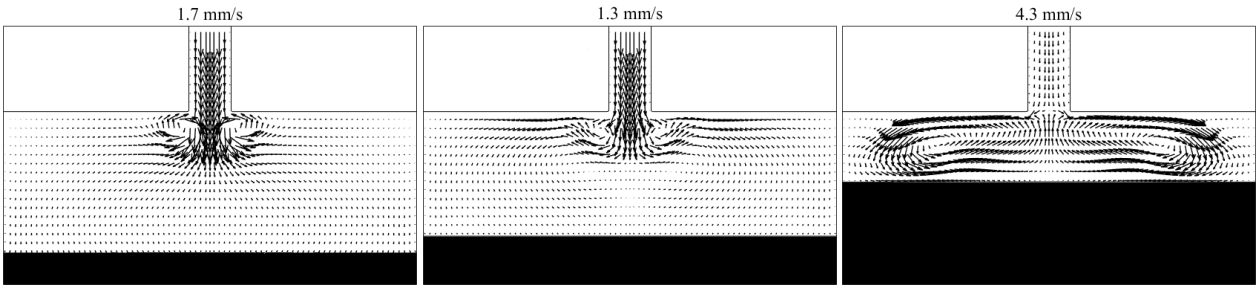

Figure 4.9 : Solidification phenomenon for Cu at times (a) 10 s, (b) 24 s, and (c) 100 s

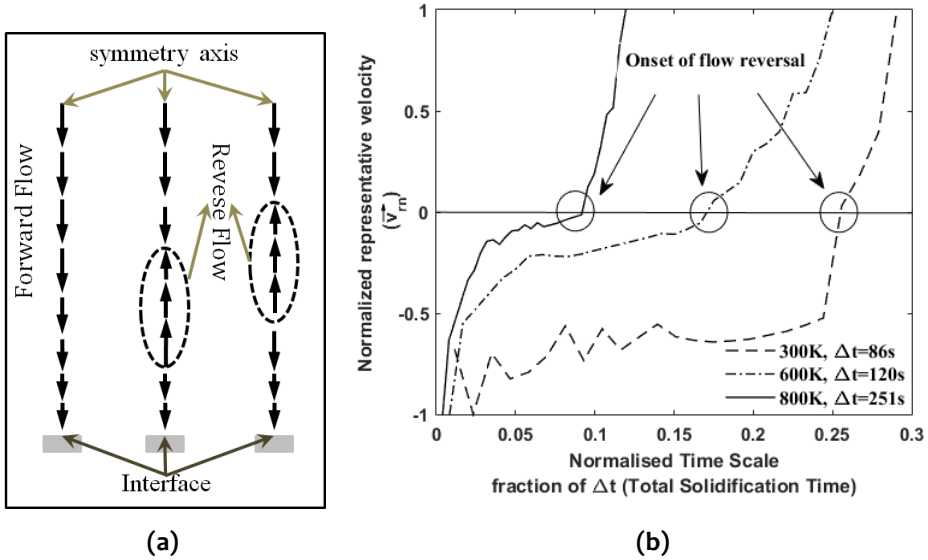

Figure 4.10 : (a) Schematic representation of velocity vectors along central symmetry line for forward and reverse flow (b) Onset of flow reversal for varying cold boundary temperature T_c on the normalized time scale

these counter rotating convection cells reverse their direction, causing a net upward flow along the central plane toward the riser opening due to the effect of buoyancy. However, the magnitude of maximum velocity due to shrinkage induced flow during the directional solidification of Cu is found to be higher as compared to case study associated with Al. Since the density difference between solid and liquid phases ($\rho_s - \rho_l$) of Cu ($\approx 909\ kg/m^3$) is much larger than Al ($\approx 165\ kg/m^3$), the shrinkage induced pull is expected to be much more in case of solidification of Cu, leading to larger velocity magnitudes.

Effect of varying cold boundary temperature

This study is conducted for directional solidification of Al with bottom cooled orientation considering three different cooling temperatures applied at the bottom surface viz. 300 K, 600 K, and 800 K, while keeping the same geometrical constraints of the cavity provided in table 4.1. One of the major objectives of this study is to analyze the onset of flow reversal phenomena with respect to the normalized time scale for solidification. Colder the bottom surface temperature faster is the solidification rate. The time duration required for the completion of solidification in the cavity for each cold boundary condition is predicted and considered to be 100%. The time scale is normalized by dividing time with total time duration to accomplish complete solidification in the cavity for individual cold boundary temperatures. This method enabled us to predict the percentage of total time duration the liquid melt encounters the forward (figure 4.5 (a)) and reverse (figure 4.5 (b)) convection pattern. A close inspection of velocity fields presented in figure 4.4

and figure 4.9 reveals all the velocity vectors along the central symmetry line of the cavity are pointing in the downward direction when forward flow condition (figure 4.5 (a)) prevails. On the other hand, all velocity vectors in a bounded region along the central symmetry line manifest upward fluid movement during reverse flow condition. The location of this bounded sub-region with upward pointing velocity vector may vary along the central line span depending on varying cold boundary conditions, initial conditions and cavity aspect ratio. Nevertheless, this particular flow feature always prevails under the reverse flow condition. In essence, when all velocity vectors along the central symmetry line are pointing in the downward direction, we have forward flow condition (figure 4.5(a)); and all velocity vectors within a bounded sub-region along the central symmetry line pointing upward signifies reverse flow condition (figure 4.5 (b)). A magnified view of velocity vectors along central symmetry plane for forward and reverse flow is illustrated in figure 4.10(a). The onset of flow reversal phenomena can be apprehended by sudden change of velocity vector direction from down to up for a bounded sub-region along the central symmetry line. A sorting algorithm is used at each time instants to identify the direction of velocity vectors along the symmetry line. If all the vectors point in the downward direction ($-ve$ v component), the velocity at the midpoint between the interface and the upper surface of the cavity is stored for that particular time instant. On the other hand, if a bounded sub-region is identified with upward velocity vectors ($+ve$ v component) the velocity at the midpoint of the sub-region is stored for that time instant. This sorting process at progressive time intervals enables us to obtain a single representative velocity vector ($\vec{\mathbf{v}}_{ref}$) for each time instant in such a way that the sign of this single velocity vector solely determines whether the flow phenomena is forward or reverse. This sorting process also leads to easy identification of the time instant when the sign of the $\vec{\mathbf{v}}_{ref}$ changes from $-ve$ to $+ve$ denoting the onset of flow reversal process. It is pertinent to mention here that the sign of the $\vec{\mathbf{v}}_{ref}$ emphasises the onset of flow reversal, while the magnitude is of no consequence whatsoever. Therefore, the magnitude of the $\vec{\mathbf{v}}_{ref}$ is normalized within a range of ± 1 to describe the flow reversal phenomena in figure 4.10(b). The normalized representative velocity vector $\vec{\mathbf{v}}_{rn}$ is defined in the following manner:

$$\vec{\mathbf{v}}_{rn} = \begin{cases} \vec{\mathbf{v}}_{ref}/|\vec{\mathbf{v}}_{ref}^{min}| & \text{if } \vec{\mathbf{v}}_{ref} < 0 \\ \\ \vec{\mathbf{v}}_{ref}/|\vec{\mathbf{v}}_{ref}^{max}| & \text{if } \vec{\mathbf{v}}_{ref} > 0 \end{cases} \tag{4.24}$$

The onset of flow reversal with respect to the normalized time scale is presented in figure 4.10 for varying cold boundary temperatures. The ordinate of figure 4.10 represents normalized representative velocity vector ($\vec{\mathbf{v}}_{rn}$) defined by Eq. 4.24 and the abscissa represents the normalized solidification time scale. In this plot the normalized time instant at which the sign of $\vec{\mathbf{v}}_{rn}$ changes from $-ve$ to $+ve$, designates the onset of flow reversal. As is evident from figure 4.10, faster cooling rate associated with colder bottom surface temperature delays the flow reversal phenomena. For instance, cold boundary temperature 800 K causes more than 90% of the total solidification time to be dominated by reverse flow pattern, while with $T_c = 300$ K the reverse flow pattern is encountered during the last 75% of the total solidification duration.

Effect of varying Initial conditions

For bottom cooled configuration buoyancy force opposes the shrinkage induced flow. Since the local buoyancy source term depends on $\Delta T = T - T_{ref}$, the initial temperature of the liquid melt is expected to play a key role in defining the evolution of this source term. Also, the flow reversal phenomena being identified as a direct consequence of opposing buoyancy source term, we intend to study the effect of varying initial temperature on the onset of flow reversal. Three different initial temperature of the Al melt ($T_i = 1073$, 1223, and 1373 K with an increment of 150 K) is considered. The cold boundary temperature (T_c) is maintained at fixed value of 800 K, and the cavity-riser size

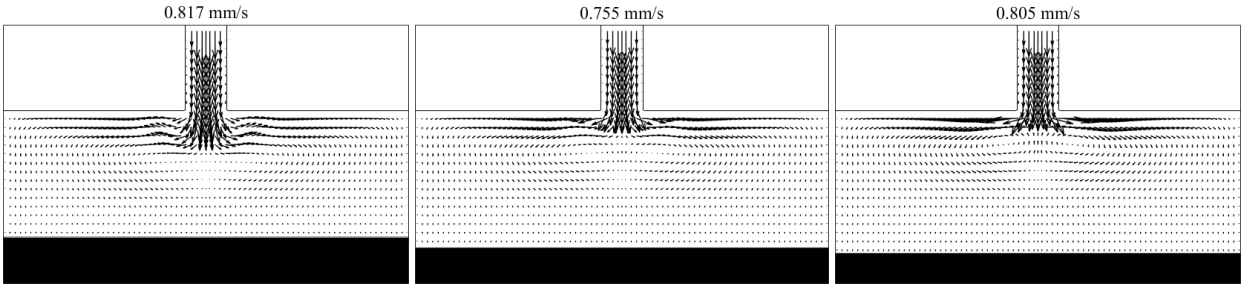

(a) (b) (c)

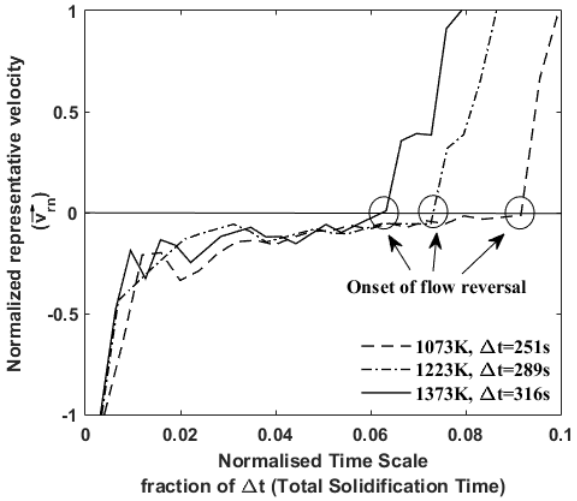

(d)

Figure 4.11 : Onset of flow reversal for varying initial condition (a) $T_i = 1073\ K$, (b) $T_i = 1223\ K$, (c) $T_i = 1373\ K$ and (d) Mapping of flow reversal for varying initial condition on the normalized time scale

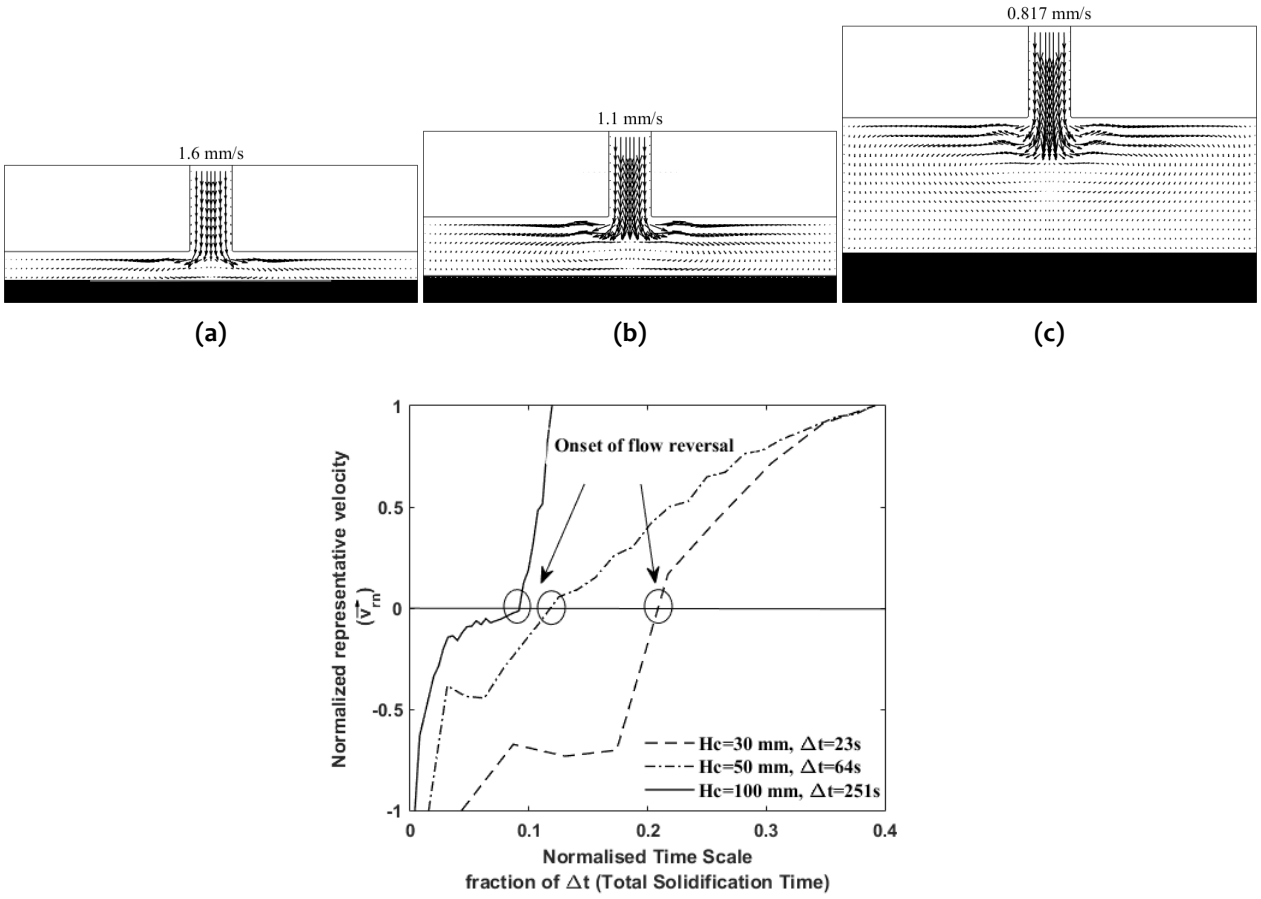

Figure 4.12 : Onset of flow reversal for varying cavity heights: (a)$H_C = 30\ mm$, (b)$H_C = 50\ mm$, (c) $H_C = 100\ mm$ and (d) Mapping of flow reversal for varying casting height on the normalized time scale

and shape is kept unaltered (refer table 4.1 and figure. 4.1). Figure 4.11(a), (b), and (c) show the snap-shots of the velocity profile in the cavity during the onset of flow reversal for different initial conditions respectively. Higher the initial temperature of the melt slower is the solidification rate. An analysis akin to the one with varying cold boundary (T_c) condition and presented by figure 4.10 on the onset of flow reversal with respect to the normalised time scale is carried out for varying initial temperatures (T_i). Figure 4.11(d) shows the onset of flow reversal on a normalised time scale *Vs.* $\vec{\mathbf{v}}_{rn}$ plot. Once again in figure 4.11(d), sign change of $\vec{\mathbf{v}}_{rn}$ from $-ve$ to $+ve$ designates the onset of flow reversal in normalized time scale framework for corresponding initial temperatures. As is evident from figure 4.11(d), higher initial temperature promotes relatively faster attainment of flow reversal in normalised time scale representation.

Effect of varying cavity height

The parametric study is concluded with the effect of cavity height on the onset of flow reversal during the directional solidification of pure Al in a bottom cooled cavity. In bottom cooled configuration the thickness of the stably stratified melt (higher density of melt at bottom and lower density at top) increases with increasing cavity height. As a result the shrinkage induced downward movement of melt from the riser along the center line of the cavity is expected to encounter more resistance for increased cavity height. For this analysis the constant temperature boundary condition (T_c) and initial temperature of the the melt (T_i) are kept at fixed values of 800 K and 1073 K respectively, while the cavity height is varied keeping the cavity width(W_c), riser size and casting conditions unaltered (refer table 4.1 and figure. 4.1). Three different cavity

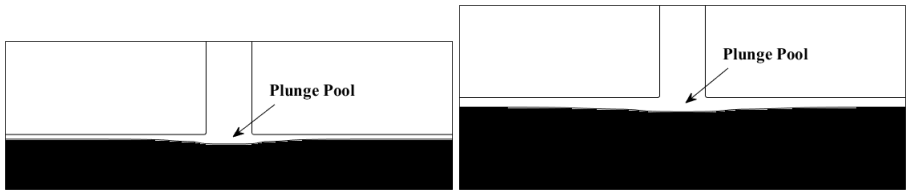

Figure 4.13 : Solid-liquid interface deformation in the form of plunge pool adjacent to riser opening to the cavity for (a) $H_c = 30\ mm$, and (b) $H_c = 50\ mm$

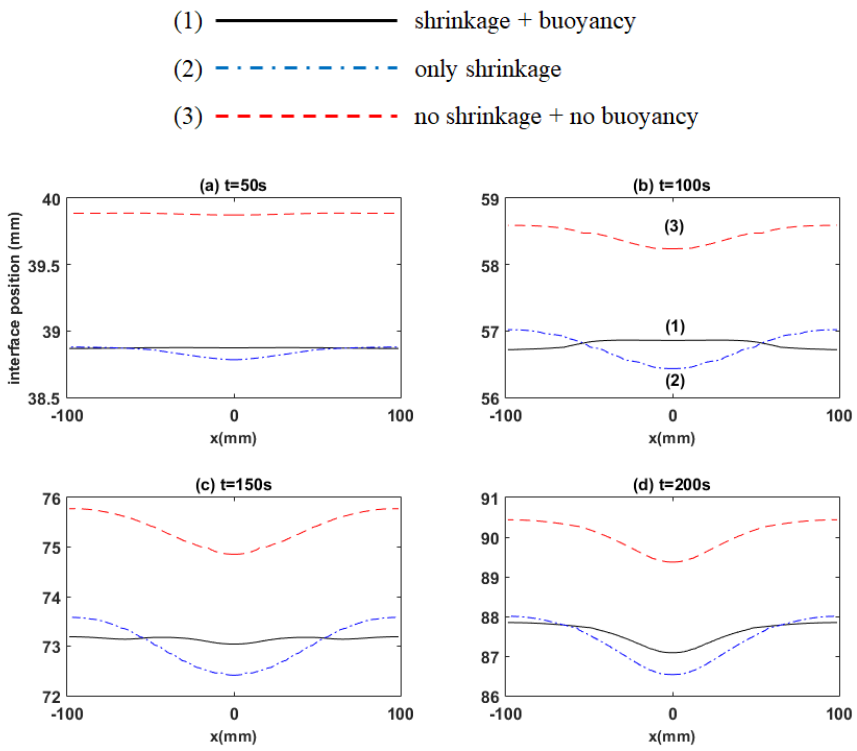

Figure 4.14 : Comparison between interface positions for different cases at different times. Plots (1), (2) and (3) represents cases with (shrinkage + buoyancy), (only shrinkage), and (no shrinkage + no buoyancy).

heights: $H_c = 30\ mm$, $H_c = 50\ mm$ and $H_c = 100\ mm$ are considered for this analysis. Figure 4.12(a), (b), and (c) show the snap-shots of the velocity profile in the cavity during the onset of flow reversal for different cavity heights respectively. Larger the cavity height greater is the resistance to the shrinkage induced flow. A similar analysis to those with varying T_c and T_i on the onset of flow reversal in a normalised time scale framework is carried out for varying cavity height (H_c). Figure 4.12(d) shows the onset of flow reversal on a normalised time scale *Vs.* $\vec{\mathbf{v}}_{rn}$ plot. Once again in figure 4.12(d), sign change of $\vec{\mathbf{v}}_{rn}$ from $-ve$ to $+ve$ represents the onset of flow reversal in normalized time scale framework for corresponding cavity heights. As is evident from figure 4.12(d), larger cavity height causes early flow reversal.

Finally, deformation of otherwise planner interface growth due to shrinkage induced flow is presented in figure 4.13 for two different cavity heights viz. 30 *mm* and 50 *mm*. The bottom boundary condition and initial temperature of the Al melt are considered to be $T_c = 800\ K$ and $T_i = 1073\ K$. Figure 4.13(a) and (b) clearly show formation of plunge-pool adjacent to the location of the riser opening to the cavity. Although, this deformation of the planer front is marginal for pure Al, we might expect it to be more significant during alloy solidification leading to interesting compositional segregation. Similarly, a comparison between interface movements for different

cases at different times using pure aluminium is shown in figure 4.14: case 1 - shrinkage + buoyancy; case 2 – only shrinkage induced flow; case 3 - no shrinkage + no buoyancy (pure diffusion model). Figure 4.14 (a)-(d) shows the shape of the solid-liquid interface adjacent to the symmetry line at different stages of solidification at various time intervals with reference to figure 4.3 and 4.4. Although the interface pattern is similar for the case 2 and 3, case 1 involving combined shrinkage and buoyancy effect shows significant difference because of the flow reversal phenomena manifested by this condition. Although the presence of plunge pool around the riser section is common for all the cases at time interval 200 *s*, depth of the plunge pool at the final stage of solidification is found to be varying for these three cases with case 1 manifesting minimum plunge pool depth. Thus, it is evident that the above study is of considerable importance in the direction of modeling and predicting compositional heterogeneity during the bottom-up solidification of the alloy system. The next chapter of the investigation is mostly dedicated to analysing the flow characteristic occurring due to heavier or lighter solute rejection.

4.6 SUMMARY

A numerical model is proposed for predicting shrinkage induced flow during directional solidification of pure and amorphous materials in a bottom cooled cavity. The system of governing equations are considered and modified to incorporate shrinkage effect by implementing volume averaging method. A novel volume fraction updating method is proposed to track the distinct interface during solidification of pure material. For bottom cooled configuration, buoyancy source term is found to play a significant role in defining the convection pattern. The shrinkage induced flow is opposed by otherwise stably stratified density gradient, leading to a distinct flow reversal phenomena during the directional solidification in bottom cooled configuration. For low Prandtl number materials like aluminium and copper, deformation of isotherms adjacent to the undulated solid-liquid interface causes the buoyancy force aided with shrinkage induced inertia to lift the fluid vertically upward along the symmetric center line of the cavity leading to the sustenance of the flow reversal. Flow reversal does not occur till the central depression of the solid-liquid interface is evolved. On the other hand, for high Prandtl substances like coconut oil, perturbation of thermal field due to shrinkage induced flow field is easily attained. As a result, an early onset of flow reversal can be observed almost coinciding with the very inception of solid front growth. The major outcome of the proposed model in terms of flow reversal phenomena is experimentally validated considering the directional solidification of coconut oil in a bottom cooled cavity. Experimentally measured flow field and liquid-mushy interface locations are compared with 3-D numerical predictions with reasonable agreements. 2-D numerical studies are performed for the directional solidification of two different pure metals namely Al and Cu. Both case studies revealed the onset and sustenance of flow reversal during the solidification process. Effect of varying cold boundary temperature, initial temperature of melt, and cavity height on the onset of flow reversal is studied for bottom cooled directional solidification of pure Al. Increase in all these three parameters is found to promote an early flow reversal when time scale is normalised with respect to the total solidification time. The shrinkage induced flow field is found to cause deformation of the planer solid front in the form of a plunge pool. For the square riser, the shape of the plunge pool is found to have distinct orientation along the length and width of the cavity. The investigation provides a strong base to further predict macro-scale shrinkage defects and the compositional heterogeneity during directional solidification of the alloy system and is discussed in succeeding chapter.

…